

In the format provided by the authors and unedited.

Probing nanoscale fluctuation of ferromagnetic meta-atoms with a stochastic photonic spin Hall effect

Bo Wang , Kexiu Rong, Elhanan Maguid , Vladimir Kleiner and Erez Hasman  

Micro and Nanooptics Laboratory, Faculty of Mechanical Engineering and Russell Berrie Nanotechnology Institute, Technion, Israel Institute of Technology, Haifa, Israel. ✉e-mail: mehasman@technion.ac.il

Probing nanoscale fluctuation of ferromagnetic meta-atoms with a stochastic photonic spin Hall effect

Bo Wang, Kexiu Rong, Elhanan Maguid, Vladimir Kleiner and Erez Hasman*

5

This supplementary information file includes:

- Section 1: Simulation and calculation of Kerr rotations and PSHEs
- 10 Section 2: Theory of weak measurement for magnetized disordered metasurfaces
- Section 3: The hystereses of PSHEs
- Section 4: The magnetic-controlled optical vortex pairs
- Section 5: The stochastic behavior of the PSHE
- 15 Section 6: Estimation of the standard deviation of PSHE from limited number of statistical measurements

Supplementary Figs. 1 to 10

20 **References**

Section 1: Simulation and calculation of Kerr rotations and PSHEs

To calculate the magneto-optical responses for a lattice of nickel nanoantennas, we conduct the simulations using the finite-difference time-domain (FDTD) method. Supplementary Fig. 1 depicts a unit of the simulation geometry. The circular nickel nanoantenna with a radius R stands on a silica substrate. The side length of the unit is $p = 400$ nm, and periodic boundary conditions are employed in the x and y directions. The height of the nanoantenna is $h = 170$ nm. The magneto-optical effects are introduced by the magnetization-controlled dielectric tensor of the ferromagnetic medium. The external magnetic field B is applied in the z direction, i.e., a polar configuration. Correspondingly, the dielectric tensor of nickel is:

$$\epsilon_{Ni} = \begin{pmatrix} \epsilon & -i\epsilon QM & 0 \\ i\epsilon QM & \epsilon & 0 \\ 0 & 0 & \epsilon \end{pmatrix},$$

where $\epsilon = n^2$; $n = 1.9 - 4i$ is the complex refractive index of nickel at a wavelength of 632.8 nm. The magneto-optical parameter is $Q = (8.5 + 6.5i) \times 10^{-3}$ [1], and M is a normalized magnetization that changes between -1 and 1 . Before magnetization ($M = 0$), there are no nondiagonal components for the dielectric tensor. Once magnetized, the anti-symmetric nondiagonal components emerge, and macroscopically, magneto-optical effects occur.

We calculated the reflection coefficients of the structure as a function of the nanoantenna radius R by impinging an x -polarized plane wave onto the structure at a normal angle with $M = 1$. The results are depicted in Fig. 2a of the main text. Generally, the reflection coefficients of the magnetized structure are described by a Jones matrix, which connects the incident and reflected waves by

$$\begin{bmatrix} E_{x,R} \\ E_{y,R} \end{bmatrix} = \begin{bmatrix} r_{xx} & r_{xy} \\ r_{yx} & r_{yy} \end{bmatrix} \begin{bmatrix} E_{x,I} \\ E_{y,I} \end{bmatrix}.$$

Here, $E_{x,I}$ and $E_{y,I}$ are the incident electric fields for x and y polarizations, and $E_{x,R}$ and $E_{y,R}$ are the reflected fields. The cross-polarized components r_{xy} and r_{yx} , generated by the magneto-optical effects, are very small compared to r_{xx} and r_{yy} . Note that we have $r_{xy} = r_{yx}$, $r_{yy} = -r_{xx}$ as the symmetric properties of the dielectric tensor [2]. For different radii R , there is also a resonant phase $\phi_0 = \text{Arg}[r_{xx}]$. The Kerr rotation is defined as $\theta_K = \text{Re}[-r_{xy}/r_{xx}]$, and the Kerr ellipticity is $\xi_K = \text{Im}[-r_{xy}/r_{xx}]$. The strength of the cross-polarization is linear to the magnetization M , namely, $r_{xy} \propto M$. Therefore, we also have $\theta_K \propto M$. For an opposite magnetization of M , the sign of θ_K flips, indicating an anti-symmetric property: $\theta_K(M) = -\theta_K(-M)$. In this work, we concentrate only on the phase effect; therefore, the Kerr ellipticity is omitted to simplify the analysis. Using these approximations, the Jones matrix can be rewritten as

$$\mathbf{J} = \begin{bmatrix} r_{xx} & r_{xy} \\ r_{yx} & r_{yy} \end{bmatrix} \approx r_{xx} \begin{bmatrix} 1 & -\sin \theta_K \\ -\sin \theta_K & -1 \end{bmatrix} \approx r_{xx} \begin{bmatrix} \cos \theta_K & -\sin \theta_K \\ -\sin \theta_K & -\cos \theta_K \end{bmatrix},$$

for $\theta_K \ll 1$. Furthermore, we can transform the Jones matrix into the photonic spin basis $|\sigma_{\pm}\rangle$ via $\mathbf{J}_{\sigma} = \mathbf{U}\mathbf{J}\mathbf{U}^{-1}$, resulting in

$$\mathbf{J}_{\sigma} = r_{xx} \begin{bmatrix} 0 & e^{-i\theta_K} \\ e^{i\theta_K} & 0 \end{bmatrix}. \quad (\text{S1})$$

5 Here $\mathbf{U} = [1 \ i; 1 \ -i]/\sqrt{2}$ is a unitary conversion matrix. From the expression of \mathbf{J}_{σ} , we have $|\sigma_{\pm}\rangle \rightarrow e^{\pm i\theta_K} |\sigma_{\mp}\rangle$ for incident spin states $|\sigma_{\pm}\rangle$ reflecting from the structure. Therefore, a geometric phase, $\phi_g = \sigma_{\pm}\theta_K$, is imparted to the flipped spin state due to the magneto-optical effect, i.e., the Berry-Zak phase. Compared to the geometric phase arising from anisotropic nanoantennas with space-variant in-plane orientations [3], the Berry-Zak phase in Eq. (S1) is
 10 from the time-reversal symmetry breaking of the light-matter interaction, rather than the spatial symmetry breaking. The magnetic field also provides a dynamic approach to tailor the strength of the geometric phase.

Once we have obtained the magneto-optical responses of the nickel nanoantennas from the FDTD simulation, we can sample the nanoantennas in a lattice with a random function $f(x, y)$,
 15 composing a disordered metasurface with spatial fluctuation of the meta-atoms (nanoantennas). Specifically, we set $R(x, y) = R_0 + \Delta R \cdot f(x, y)$. Here, (x, y) are the locations of the nanoantennas, R_0 is the average radius, ΔR is the range of fluctuation, and $f(x, y)$ is a random function with a flat probability distribution, as depicted in Supplementary Fig. 2. At each lattice point of the metasurface, the reflection and Kerr rotation can be derived from Fig. 2a in the main
 20 text via the radius R of the meta-atom. By this means, the near field and momentum space of light reflecting from the disordered metasurface can be calculated via the Huygens Principle and Fourier transformation, respectively.

For a specific realization of $f(x, y)$ and a magnetization of M , we obtain the corresponding resonant phases $\phi_0(x, y)$ and the geometric phases $\phi_g = \sigma_{\pm}\theta_K(x, y)$ of light reflected from the
 25 disordered metasurface. The spin-dependent intensity distributions of light $I_{\sigma_{\pm}}(k_x, k_y)$ in the momentum space (k_x, k_y) are calculated by Fourier transformation. Note that in this work, (k_x, k_y) are always normalized by the wavenumber of the incident light, $k_l = 2\pi/\lambda$. The spin shift of light in the momentum space, i.e., the PSHE, is defined as

$$\delta_{x,y} = \frac{\int k_{x,y} I_{\sigma_+}(k_x, k_y) dk_x dk_y}{\int I_{\sigma_+}(k_x, k_y) dk_x dk_y} - \frac{\int k_{x,y} I_{\sigma_-}(k_x, k_y) dk_x dk_y}{\int I_{\sigma_-}(k_x, k_y) dk_x dk_y},$$

in the x and y directions, respectively. The PSHE is also indicated by a nonzero S_3 distribution

$$S_3(k_x, k_y) = \frac{I_{\sigma_+}(k_x, k_y) - I_{\sigma_-}(k_x, k_y)}{I_{\sigma_+}(k_x, k_y) + I_{\sigma_-}(k_x, k_y)}.$$

Examples of the calculation are shown in Supplementary Fig. 3 for 1D disordered
 5 metasurfaces with $R(x) = R_0 + \Delta R \cdot f(x)$. Two different realizations of $f(x)$ are depicted in the
 left (a) and right (b) panels of Supplementary Fig. 3. The disordered resonant phases $\phi_0(x)$ are
 spin-independent; hence, they do not cause any photonic spin shift. The PSHE arises from the
 spin-dependent geometric phases. Obviously, for different realizations of $f(x)$, we obtain distinct
 spin shifts. To achieve a larger PSHE, R_0 should be in the resonant region to introduce a stronger
 10 fluctuation of Kerr rotations and geometric phases. Therefore, in our fabrications, we chose $R_0 =$
 115 nm, which is located in the resonant region, as we simulated. To demonstrate the resonant
 effect, we measured the reflection spectrum of the fabricated 1D disordered metasurface for
 wavelengths ranging from 600 nm to 700 nm, as shown in Supplementary Fig. 4. The decrease in
 the reflection around the wavelength of 632.8 nm (the working wavelength for the PSHE)
 15 indicates a resonant effect.

Section 2: Theory of weak measurement for magnetized disordered metasurfaces

The weak measurement setup shown in Fig. 3a of the main text is a typical approach to detect the
 PSHE. The incident beam is spatially confined, i.e., a Gaussian beam, which can be decomposed
 into a spectrum of plane waves with different directions (k_x, k_y). The off-axis illumination will
 20 introduce a background spin Hall effect (in this work, we simply call it a background effect to
 distinguish it from the PSHE we are interested in) [4, 5]. Therefore, it is crucial in the
 measurement to distinguish the background effect from the PSHE purely arising from the spatial
 fluctuation of the magneto-optical effects. Akin to Ref [4], here we show that for a Gaussian
 beam, the wavevector dependent polarization rotation upon reflection at the metaurface. The
 25 eigenstates of polarization for an off-axis beam impinging onto a metasurface are P and S, which
 correspond to the cases with the electric field in and out of the plane of incidence, respectively
 (Supplementary Fig. 5a). Note that P and S are only the eigenstates of a single plane wave,
 namely, for the center wavevector (k_i) of a Gaussian beam. For different plane wave component
 of the Gaussian beam, different eigenstates \bar{p}, \bar{s} are attached (Supplementary Fig. 5a).
 30 Considering the geometric constrains, there is a relation between P, S and \bar{p}, \bar{s} for an arbitrary
 plane wave component:

$$\mathbf{P} = \bar{p} - k_y \bar{s} \cot \alpha, \mathbf{S} = \bar{s} + k_y \bar{p} \cot \alpha, \quad (\text{S2})$$

with α being the incident angle and k_y being the normalized wavenumber denoting the direction of the plane wave component. Note that for reflected wave, α should be replaced by $-\alpha$ [6,7]. On the other hand, \bar{p}, \bar{s} states are also combinations of their associated spin states

$$5 \quad \bar{p} = |\sigma_+\rangle + |\sigma_-\rangle, \bar{s} = \frac{1}{i} (|\sigma_+\rangle - |\sigma_-\rangle). \quad (\text{S3})$$

When a P-polarized beam reflecting from an interface, each plane wave reflects independently with its own reflection coefficient. In the case of a homogeneously magnetized metasurface, we have

$$\begin{aligned} \mathbf{P} &= \bar{p} - k_y \bar{s} \cot \alpha \xrightarrow{\text{Reflection}} (\bar{r}_p \bar{p} + \bar{r}_{ps} \bar{s}) - k_y (\bar{r}_s \bar{s} + \bar{r}_{sp} \bar{p}) \cot \alpha \\ &= (\bar{r}_p - \bar{r}_{sp} k_y \cot \alpha) \bar{p} + (\bar{r}_{ps} - \bar{r}_s k_y \cot \alpha) \bar{s} \\ &\approx \bar{r}_p \mathbf{P} + [-k_y (\bar{r}_s + \bar{r}_p) \cot \alpha + \bar{r}_{ps}] \mathbf{S}. \end{aligned}$$

10 Here, \bar{r}_p and \bar{r}_s are the homogeneous reflection coefficients of light for the p and s polarizations, respectively, and the component \bar{r}_{ps} is the cross-polarization generated from the homogeneous magneto-optical effect. Here we considered the approximation that both k_y and \bar{r}_{sp} are small quantities compared to \bar{r}_p , so the term containing $k_y \bar{r}_{sp}$ is omitted. Up to now, the background effects have shown. They arise from the cross polarization generated from different plane waves
15 k_y in the reflection.

The PSHE induced by the disordered magneto-optical effects has a different origin from the background effects: it is induced by the space-variant geometric phases. Therefore, in this effect, the eigenstates of polarization are the spin states, rather than \bar{p} and \bar{s} . Approximately, this PSHE is independent from different plane wave component in the Gaussian beam. Considering
20 only a spin shift in the y direction, δ_y , we have

$$e^{\frac{k_y^2}{k_w^2}} |\sigma_\pm\rangle \xrightarrow{\text{disordered MO effects}} e^{-\frac{1}{k_w^2} \left(k_y \pm \frac{\delta_y}{2}\right)^2} |\sigma_\pm\rangle \approx e^{\frac{k_y^2}{k_w^2} \left(1 \mp \frac{k_y \delta_y}{k_w^2}\right)} |\sigma_\pm\rangle. \quad (\text{S4})$$

Note that $k_w = k_l \lambda / D$ is the diffraction limit. Combing Eq. S3 and Eq.S4, we have

$$\begin{aligned}\bar{p} &= |\sigma_+\rangle + |\sigma_-\rangle \xrightarrow{\text{disordered MO effects}} \left(1 - \frac{\delta_y}{k_w^2} k_y\right) |\sigma_+\rangle + \left(1 + \frac{\delta_y}{k_w^2} k_y\right) |\sigma_-\rangle = \bar{p} - i \frac{\delta_y}{k_w^2} k_y \bar{s}, \\ \bar{s} &= \frac{|\sigma_+\rangle - |\sigma_-\rangle}{i} \xrightarrow{\text{disordered MO effects}} \frac{\left(1 - \frac{\delta_y}{k_w^2} k_y\right) |\sigma_+\rangle - \left(1 + \frac{\delta_y}{k_w^2} k_y\right) |\sigma_-\rangle}{i} = \bar{s} + i \frac{\delta_y}{k_w^2} k_y \bar{p}.\end{aligned}$$

Now taking into account both the polarization changes in the reflection and the PSHE from the disordered magneto-optical effects by combining Eq. (S2)–Eq. (S4), we have

$$\begin{aligned}\mathbf{P} &= \bar{p} - k_y \bar{s} \cot \alpha \xrightarrow{\text{Reflection}} \left[\bar{r}_P \left(\bar{p} - i \frac{\delta_y}{k_w^2} k_y \bar{s} \right) + \bar{r}_{PS} \bar{s} \right] - k_y \left[\bar{r}_S \left(\bar{s} + i \frac{\delta_y}{k_w^2} k_y \bar{p} \right) + \bar{r}_{SP} \bar{p} \right] \cot \alpha \\ &\approx \bar{r}_P \mathbf{P} + \left[-k_y (\bar{r}_S + \bar{r}_P) \cot \alpha + \bar{r}_{PS} - i \bar{r}_P \frac{\delta_y}{k_w^2} k_y \right] \mathbf{S}.\end{aligned}\quad (\text{S5})$$

- 5 Here, the origin of δ_y is the disordered magneto-optical effects. That is, $\delta_y \sim \Delta(r_{PS} / r_P)$, which denotes the spatial fluctuation of r_{PS} / r_P . The effects in the weak measurements from different sources are presented by the three terms in the S state in Eq. (S5). Specifically, the first term, $-k_y (\bar{r}_S + \bar{r}_P) \cot \alpha$, is the background effect from the off-axis reflection from a homogeneous surface; the second term, \bar{r}_{PS} , is the effect from the homogeneous magneto-optical effect; and the
- 10 third term, $-i \bar{r}_P \delta_y k_y / k_w^2$, is the PSHE that we are interested in—one purely arising from the spatial fluctuation of magneto-optical effects. As we will show, an important approach to distinguish the three different effects is to exploit different symmetric properties of these effects in the weak measurement via changing the magnetic field.

The electric field distribution after the postselection is

$$15 \quad E(k_y, \beta) = \begin{bmatrix} \sin \beta & 0 \\ 0 & \cos \beta \end{bmatrix} \begin{bmatrix} 1 & 0 \\ 0 & i \end{bmatrix} \begin{bmatrix} \bar{r}_P \\ -k_y (\bar{r}_S + \bar{r}_P) \cot \alpha + \bar{r}_{PS} - i \bar{r}_P \frac{\delta_y}{k_w^2} k_y \end{bmatrix}, \quad (\text{S6})$$

and the corresponding intensity distribution is $I_\beta(k_y) = |E(k_y, \beta)|^2$. Rewriting the expression in the two-dimensional case, we have the centroid of the beam

$$\langle k_{x,y} \rangle'_\beta = \frac{\int k_{x,y} I_\beta(k_x, k_y) dk_x dk_y}{\int I_\beta(k_x, k_y) dk_x dk_y}.$$

As we mentioned before, it is very important to study the behavior of the curves by changing the magnetic field. Therefore, we compare $\langle k_{x,y} \rangle'_\beta$ with the one obtained from zero magnetization, resulting in a modified expression:

$$\langle k_{x,y} \rangle_\beta = \langle k_{x,y} \rangle'_\beta - \frac{\int k_{x,y} I_\beta(k_x, k_y)_{M=0} dk_x dk_y}{\int I_\beta(k_x, k_y)_{M=0} dk_x dk_y}, \quad (\text{S7})$$

5 where $I_\beta(k_x, k_y)_{M=0}$ is the intensity distribution from zero magnetization.

Now, we show three different examples of the theoretical curves of $\langle k_{x,y} \rangle_\beta$ defined by Eq. (S7) with opposite magnetizations $M = \pm 1$. The first is a homogeneous surface without any magneto-optical effect, that is, $\bar{r}_{PS} = 0$ and $\Delta(r_{PS} / r_p) = 0$. The results are shown in Supplementary Fig. 5b. Clearly, without the magneto-optical effect, there is no difference between the cases before and after the surface is magnetized, and the curves are always zero. This means, that the background effect from the off-axis illumination is eliminated by this means. The results from a surface with homogenous magnetization ($\bar{r}_{PS} \neq 0$ and $\Delta(r_{PS} / r_p) = 0$) are shown in Supplementary Fig. 5c. Here, the influence of the magneto-optical effect on the weak measurement is indicated by the nonzero $\langle k_y \rangle_\beta$, which arises from \bar{r}_{PS} of the magneto-optical effect. Note that

10 $\langle k_y \rangle_{\beta, M=-1} \approx -\langle k_y \rangle_{\beta, M=1}$ due to the symmetric property $\bar{r}_{PS}(M) = -\bar{r}_{PS}(-M)$. In addition, there is a symmetric behavior with respect to β , $\langle k_y \rangle_\beta \approx \langle k_y \rangle_{-\beta}$, for each magnetization. The results of the surface with spatially fluctuating magneto-optical effects are shown in Supplementary Fig. 5d. We observe an anti-symmetric behavior with respect to β , $\langle k_y \rangle_\beta \approx -\langle k_y \rangle_{-\beta}$, which is different from the previous cases. In fact, in this weak measurement, the amplified PSHE is

$$20 \quad A_\beta \delta_{x,y} = \langle k_{x,y} \rangle_\beta - \langle k_{x,y} \rangle_{-\beta}, \quad (\text{S8})$$

with A_β being the amplification factor. Therefore, only in the third case (Supplementary Fig. 5d) do we expect a nonzero PSHE, as $\langle k_y \rangle_\beta - \langle k_y \rangle_{-\beta} \neq 0$. The exact expression of A_β can be derived from Eq. (S6). However, experimentally unknown parameters such as \bar{r}_p , \bar{r}_s and \bar{r}_{PS} are generally involved, making it unrealistic to evaluate the real spin shift from A_β . Fortunately,

25 there is a good approximation of $A_\beta \approx \bar{A}_\beta = 2 / \tan \beta$ for $|\beta| > |\beta_C|$, where the approximated amplification factor is free from the unknown parameters. Therefore, by choosing a proper β value and using Eq. (S8), the real spin shift can be evaluated. The β_C value can be determined in

the experiment via $A_\beta \delta_{x,y} / \bar{A}_\beta = \left(\langle k_{x,y} \rangle_\beta - \langle k_{x,y} \rangle_{-\beta} \right) / \bar{A}_\beta$, because for $|\beta| > |\beta_C|$,

$A_\beta \delta_{x,y} / \bar{A}_\beta = (\langle k_{x,y} \rangle_\beta - \langle k_{x,y} \rangle_{-\beta}) / \bar{A}_\beta \approx \delta_{x,y}$. Examples of the theoretical curves are shown in Supplementary Fig. 6, which are in agreement with the experimentally observed curves in Fig. 3e of the main text.

Section 3: The hystereses of PSHEs

5 For ferromagnetic materials such as nickel, the magnetization M does not respond linearly to the external magnetic field B . For instance, when the external magnetic field B abruptly disappears, a remnant magnetization still exists. In general, the magnetization of the ferromagnetic materials under a certain magnetic field can be different depending on the history of the magnetic field evolution, a phenomenon known as the hysteresis effect. Here, we demonstrate the hystereses of
 10 the PSHEs from the disordered metasurfaces of ferromagnetic meta-atoms, as shown in Supplementary Fig. 7. The measurements are carried out starting with $B = 0$; then, B is increased in steps by 25 mT until reaching 100 mT. Next, the magnetic field B decreases to the maximum in the opposite direction, -100 mT, and so on. The revolution of the magnetic field is depicted by the arrows in Supplementary Fig. 7. The measured hystereses of PSHEs that arise from the
 15 space-variant magneto-optical effects are shown by the dots for the examples of 1D and 2D disordered metasurfaces in Supplementary Fig. 7a and b, respectively. Note that distinct behaviors of the hysteresis are observed due to the potentially complicated magneto-optical responses of different meta-atoms. As a comparison, we also measure the hysteresis of the PSHE from a homogeneous nickel film (Supplementary Fig. 7c). The observed PSHEs are much
 20 weaker, and almost swallowed up by the system noise.

Section 4: The magnetic-controlled optical vortex pairs

In solid-state systems, the topological Hall effect (THE) arises from the nontrivial interaction between electrons and a media of space-variant magnetization [8–11]. Particularly, when an electron encounters a nanoscale magnetic topological defect such as a skyrmion, THE also
 25 occurs. This phenomenon can be utilized to detect nanoscale defects by measuring the deflection of electrons.

For the disordered ferromagnetic metasurface, the PSHE arises from the space-variant magneto-optical effect, which is very similar to the space-variant magnetization for electrons. Accordingly, there should also be a similar spin shift of light related to the optical topological
 30 defects. To demonstrate this, we calculated the near field of 2D disordered metasurfaces using the Huygens Principle. That is, each meta-atom is considered as a spin- and magnetization-dependent point source emitting the electromagnetic wave into the near field of the metasurface as $|r_{xx}(x, y)| \exp(i\phi(x, y)) \cdot \exp(ik_l r_0) / r_0$, where k_l is the wavenumber and r_0 is the distance between the calculation area and the point (x, y) in the metasurface. Here $r_{xx}(x, y)$ and $\phi(x, y)$

are extracted from the FDTD calculation as mentioned in Section 1. We propagate the phase distribution $\phi(x, y) = \phi_0(x, y) + \phi_g(x, y)$ for approximately one wavelength above the metasurface and the calculated phase and intensity distributions for incident light in the $|\sigma_+\rangle$ state are shown in Supplementary Fig. 8b-d, with different external magnetic fields (in the calculation, Supplementary Fig. 8b to d correspond to $M = -1, 0$ and 1 , respectively). We obtained subwavelength-scale optical vortex pairs (VPs)—pairs of optical phase singularities with opposite topological charges—which are controlled by the magnetization. In the intensity distributions, the VPs correspond to the dark spots due to the rapid phase change in the subwavelength scale, i.e., the superoscillation of the optical field. The emergence of magnetic-controlled VPs is related to the PSHE, providing potential applications for detecting topological nanostructures via the spin shift of light. In the experiment, we fabricated a 2D disordered metasurface (Supplementary Fig. 8a) and measured the near-field intensity distributions of it under different external magnetic fields, as shown in Supplementary Fig. 8e-g. The change in the near-field intensity distributions, especially the variance of the dark spots, indicates the evolution of VPs under the change in the external magnetic field.

Section 5: The stochastic behavior of the PSHE

The stochastic behavior of the PSHE is studied by calculating the resulting spin symmetry breaking from numerous disordered metasurfaces with different realizations of the random function $f(x, y)$. For simplicity, we start with 1D disordered metasurfaces of random functions $f(x)$ to obtain important insight. In the statistical calculation, we assume that each metasurface has a size of $D \times D$, with $N \times N$ meta-atoms arranged in a square lattice with a side length of $p = D/(N-1)$. By default, the incident beam has the same size as that of the metasurface. The geometric phases (here, we consider only the values for $|\sigma_+\rangle$) from the metasurfaces are described as $\phi_g(x) = \Delta\phi_g f(x)$, where $\Delta\phi_g$ is the fluctuation range. The statistical properties of the PSHEs are entirely determined by three parameters: D , p , and $\Delta\phi_g$. Practically, $\Delta\phi_g$ is further determined by $R(x)$ of the meta-atoms and the magnetization M . However, in the calculation, we can assume some small value of $\Delta\phi_g$ to obtain the basic properties of the effects, without loss of generality.

In the statistical calculation for the disordered metasurfaces, we found a linear correlation between the spin shift δ_x and the average local geometric phase gradient \bar{K}_g (Supplementary Fig. 9a). Here, \bar{K}_g is defined as

$$\bar{K}_g = \langle \partial \phi_g / \partial x \rangle = \frac{\sum_{i=1}^{N-1} \frac{\phi_g(x_{i+1}) - \phi_g(x_i)}{p}}{\sum_{i=1}^{N-1} 1} = \frac{\phi_g(x_N) - \phi_g(x_1)}{D}, \quad (\text{S9})$$

with $x_i = ip$ being the location of the i -th meta-atom along the x axis. The probability distribution of δ_x is a Gaussian function, with a standard deviation of $\Delta\delta_x$ (Supplementary Fig. 9b). On the other hand, the probability distribution of \bar{K}_g is a triangle distribution with a standard deviation of $\Delta\bar{K}_g$ (Supplementary Fig. 9c). This particular type of probability distribution can be demonstrated from Eq. (S9). Since the geometric phases on the boundaries— $\phi_g(x_N)$ and $\phi_g(x_1)$ —are random numbers obeying a flat distribution, as depicted in Supplementary Fig. 9d. The difference between them, $\bar{K}_g D$, is also a random number. By calculations, $\bar{K}_g D$ obeys a triangle distribution, as shown in Supplementary Fig. 9e, and there is a simple relation between $\Delta\bar{K}_g$ and $\Delta\phi_g$: $\Delta\bar{K}_g \propto \Delta\phi_g / D$.

Since δ_x and \bar{K}_g are linearly correlated, we also have $\Delta\delta_x = \chi\Delta\bar{K}_g$, with χ determined by p . Combining all the relations, we obtain

$$\Delta\delta_x \propto \frac{\Delta\phi_g}{D}. \quad (\text{S10})$$

Equation (S10) describes the basic behavior of $\Delta\delta_x$, which is proportional to the spatial fluctuation of the geometric phases and inversely proportional to the size of the metasurface. Therefore, a nonzero $\Delta\delta_x$ occurs only in a spatially-bounded system with a spatial fluctuation of geometric phases, which can be generated from a wide range of fluctuation effects in physics. For the metasurfaces composed of circular ferromagnetic meta-atoms with space-variant radii, we have $\phi_g(x) = \theta_K(x)$, which is determined by M and $R(x)$. Specifically, in the resonant region shown in Fig. 2a of the main text, θ_K changes linearly with R . Therefore, we have

$$\Delta\delta_x \propto \frac{M\Delta R}{D}. \quad (\text{S11})$$

Therefore, the fluctuation (especially for nanoscale fluctuations) of meta-atoms can be evaluated by measuring the standard deviation of the probability distribution of PSHEs from Eq. (S11). These conclusions can also be generalized for 2D disordered metasurfaces.

Section 6: Estimation of the standard deviation of PSHE from limited number of statistical measurements

The calculated Gaussian distribution of the PSHE is realized by numerous different disorders ($>10^4$). However, the number (q) of samples with different disorders is experimentally limited.

- 5 Therefore, the estimated standard deviation from q measurements, $\Delta\delta^q$, has some uncertainty. We call $\Delta\delta^q$ an estimation of the standard deviation for $\Delta\delta^{q\rightarrow\infty}$ (for simplicity, it is noted as $\Delta\delta$). The standard deviation of $\Delta\delta^q$, $\Delta(\Delta\delta^q)$, divided by $\Delta\delta$, is a function of q [12]:

$$\frac{\Delta(\Delta\delta^q)}{\Delta\delta} = \frac{\Gamma\left(\frac{q-1}{2}\right)}{\Gamma(q/2)} \cdot \sqrt{\frac{q-1}{2} - \left[\frac{\Gamma(q/2)}{\Gamma\left(\frac{q-1}{2}\right)}\right]^2}. \quad (\text{S12})$$

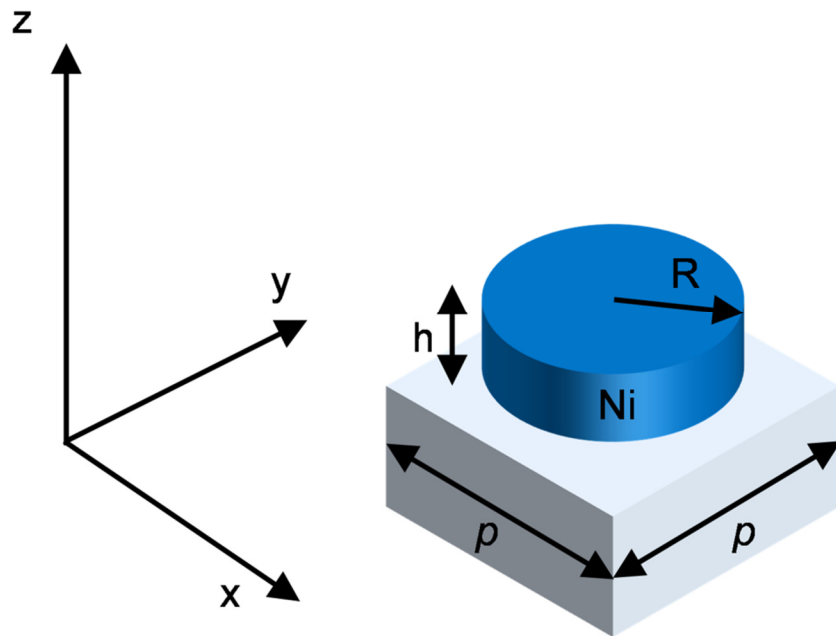
- 10 Here, $\Gamma(\cdot)$ denotes the gamma function. The curve in Supplementary Fig. 10 shows $\Delta(\Delta\delta^q)/\Delta\delta$ as a function of q . The dots are simulated results by repeating the statistical calculation for many times (10^4), with each time conducting q different disorders and resulting in a value of $\Delta\delta^q$. For $q = 30$, $\Delta(\Delta\delta^q)/\Delta\delta \approx 0.13$. Therefore, for the $q = 30$ statistical measurement, the estimated standard deviation of the PSHE should locate in the region of $[1-0.13, 1+0.13]\Delta\delta$, which is the blue area in Fig.4g of the main text.

15

References

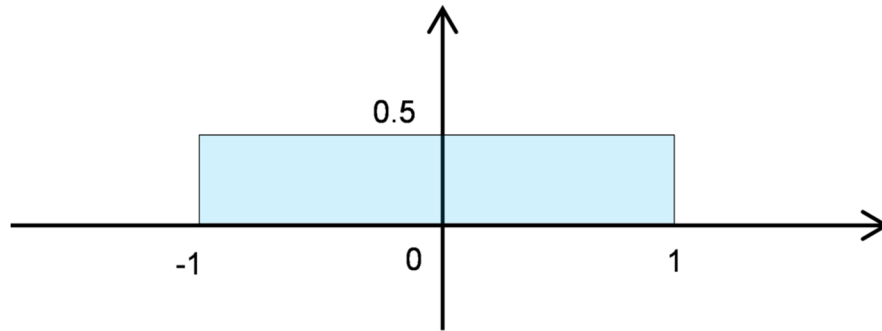
1. Goto, T., Hasegawa, M., Nishinomiya, T. & Nakagawa, Y. Temperature Dependence of Magneto-Optical Effects in Nickel Thin Films. *J. Phys. Soc. Japan* **43**, 494–498 (1977).
2. Oppeneer, P. M. Magneto-optical Kerr spectra. *Handb. Magn. Mater.* 229–422 (2001).
- 20 3. Bomzon, Z., Biener, G., Kleiner, V. & Hasman, E. Space-variant Pancharatnam–Berry phase optical elements with computer-generated subwavelength gratings. *Opt. Lett.* **27**, 1141 (2002).
4. Hosten, O. & Kwiat, P. Observation of the spin Hall effect of light via weak measurements. *Science* **319**, 787–790 (2008).
- 25 5. Bliokh, K. Y. & Bliokh, Y. P. Conservation of angular momentum, transverse shift, and spin hall effect in reflection and refraction of an electromagnetic wave packet. *Phys. Rev. Lett.* **96**, 1–4 (2006).
6. Wang, B. *et al.* Measuring spin Hall effect of light by cross-polarization intensity ratio. *Opt. Lett.* **39**, 3425 (2014).
- 30 7. Qin, Y., Li, Y., He, H. & Gong, Q. Measurement of spin Hall effect of reflected light. *Opt. Lett.* **34**, 2551–2553 (2009).

8. Schulz, T. *et al.* Emergent electrodynamics of skyrmions in a chiral magnet. *Nat. Phys.* **8**, 301–304 (2012).
9. Vistoli, L. *et al.* Giant topological Hall effect in correlated oxide thin films. *Nat. Phys.* **15**, 67–72 (2019).
- 5 10. Yin, G., Liu, Y., Barlas, Y., Zang, J. & Lake, R. K. Topological spin Hall effect resulting from magnetic skyrmions. *Phys. Rev. B* **92**, 3–7 (2015).
11. Göbel, B., Mook, A., Henk, J. & Mertig, I. The family of topological Hall effects for electrons in skyrmion crystals. *Eur. Phys. J. B* **91**, 1–8 (2018).
- 10 12. Cureton, E., The Teacher's Corner: Unbiased Estimation of the Standard Deviation, *The American Statistician*, **22**, 22 (1968).



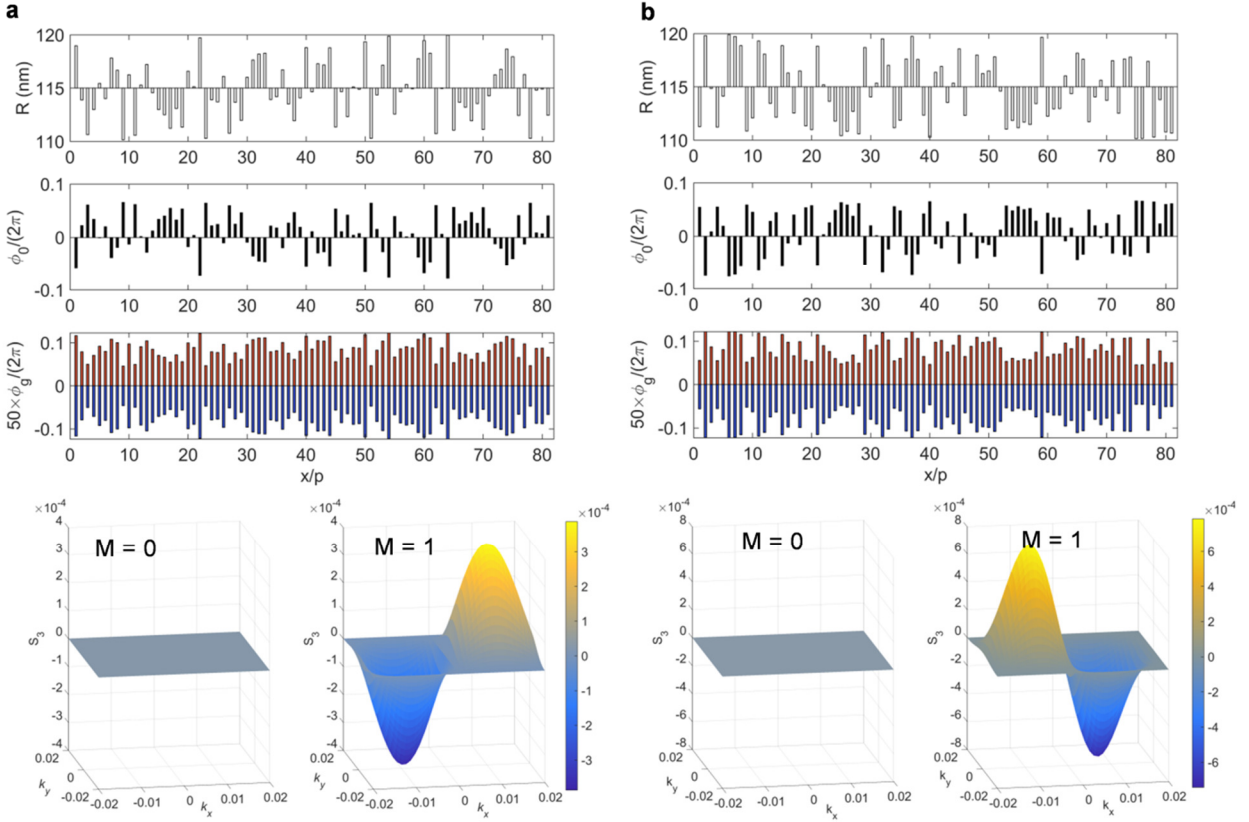
Supplementary Fig. 1. Illustration of the unit structure for simulation. A circular nickel nanoantenna sits on a fused silica substrate. The shown structure is a unit of a square lattice. In the simulation, periodic boundary conditions are applied to the sides. Light impinges onto the structure from the z direction, and the magnetic field is applied in the z direction.

The probability distribution of $f(x, y)$



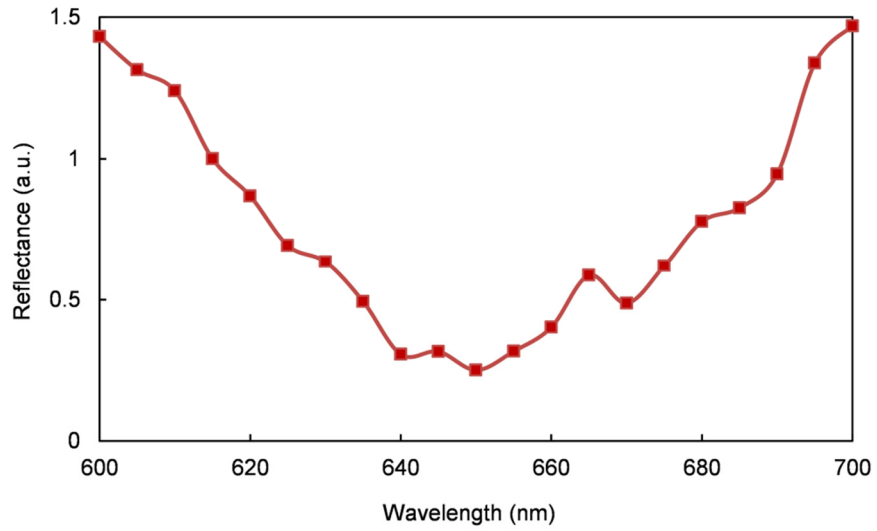
Supplementary Fig. 2. The probability distribution of the random function $f(x, y)$. At each location (x, y) , $f(x, y)$ is a random number falling in the range $[-1, 1]$ with an equal probability.

5

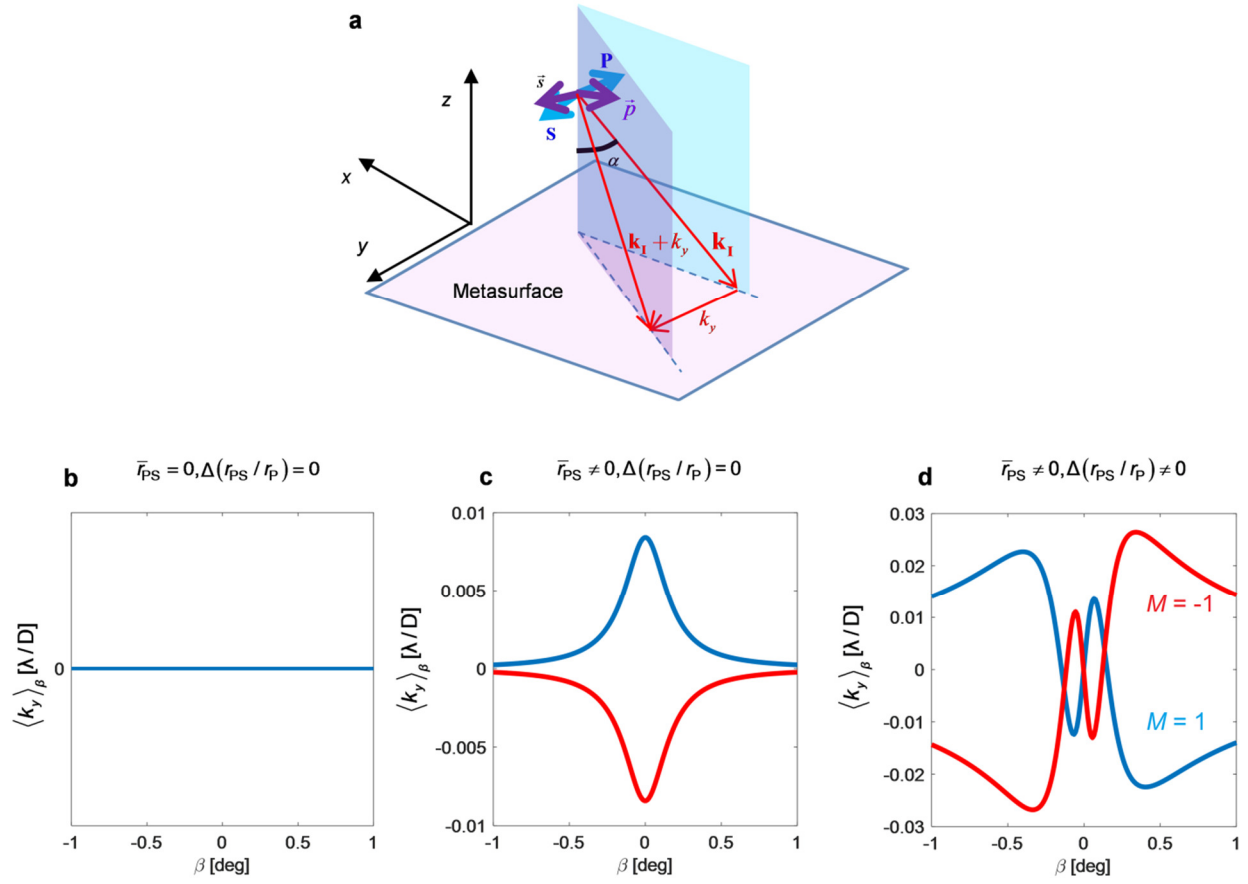


Supplementary Fig. 3. The Berry-Zak phase and PSHE from disordered ferromagnetic metasurfaces. The calculated resonant phases $\phi_0(x)$ and geometric phases $\phi_g(x)$ of 1D disordered metasurfaces with different distributions $R(x)$ (**a** and **b**).

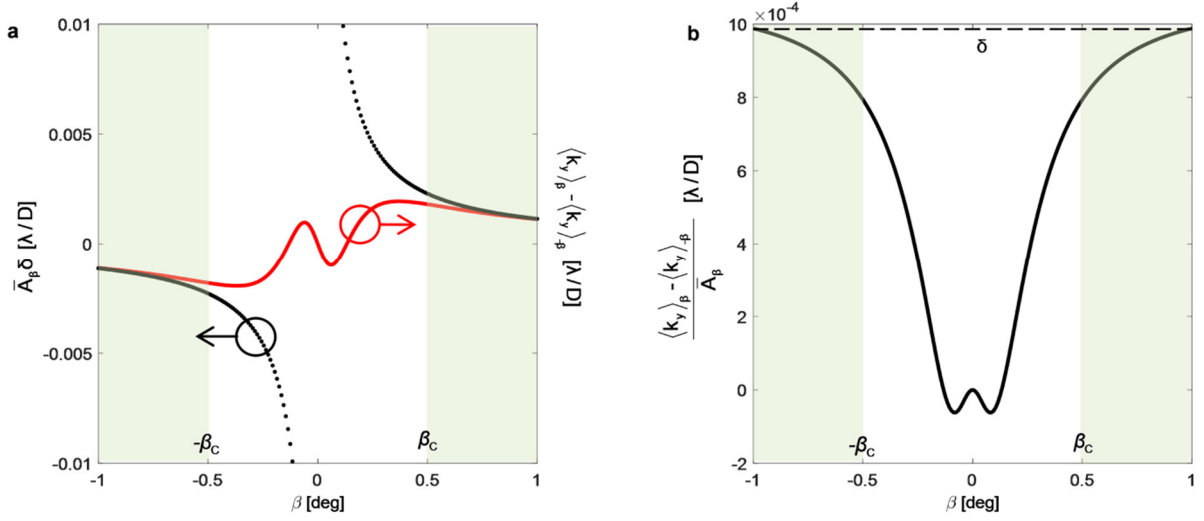
- 5 The orange and blue bars are the geometric phases obtained with $M = 1$ for $|\sigma_+\rangle$ and $|\sigma_-\rangle$, respectively. The bottom panel depicts the S_3 distributions before and after the metasurface is magnetized.



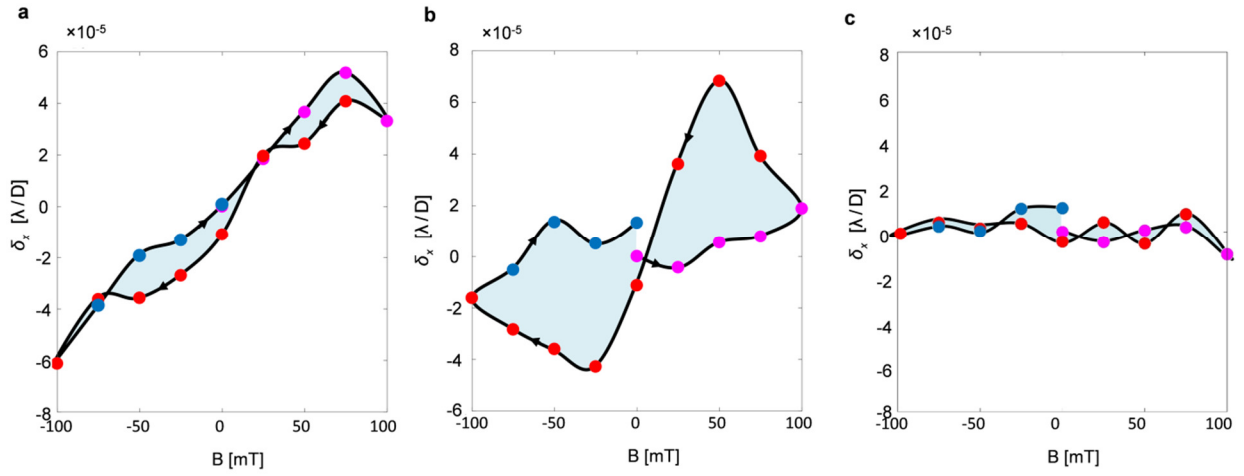
Supplementary Fig. 4. The measured reflection spectrum of a disordered metasurface. The average radius of the meta-atoms $R_0 = 115$ nm, and the range of radius fluctuation $\Delta R = 10$ nm.



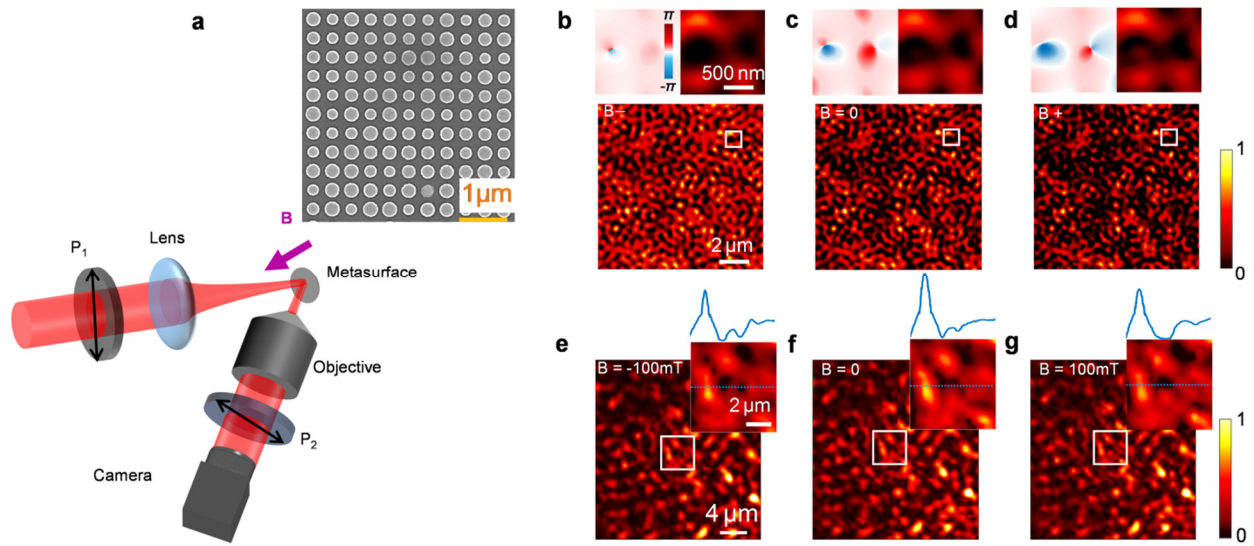
Supplementary Fig. 5. Theoretical curves of the weak measurements for different cases. **a**, Different plane waves in the incident beam, and eigenstates of polarizations. **b-d**, The modified curves $\langle k_y \rangle_\beta$ in the weak measurement for light reflecting from a homogeneous surface without the magneto-optical effect (**b**), a surface with a homogeneous magneto-optical effect (**c**), and a surface with space-variant magneto-optical effects (**d**).



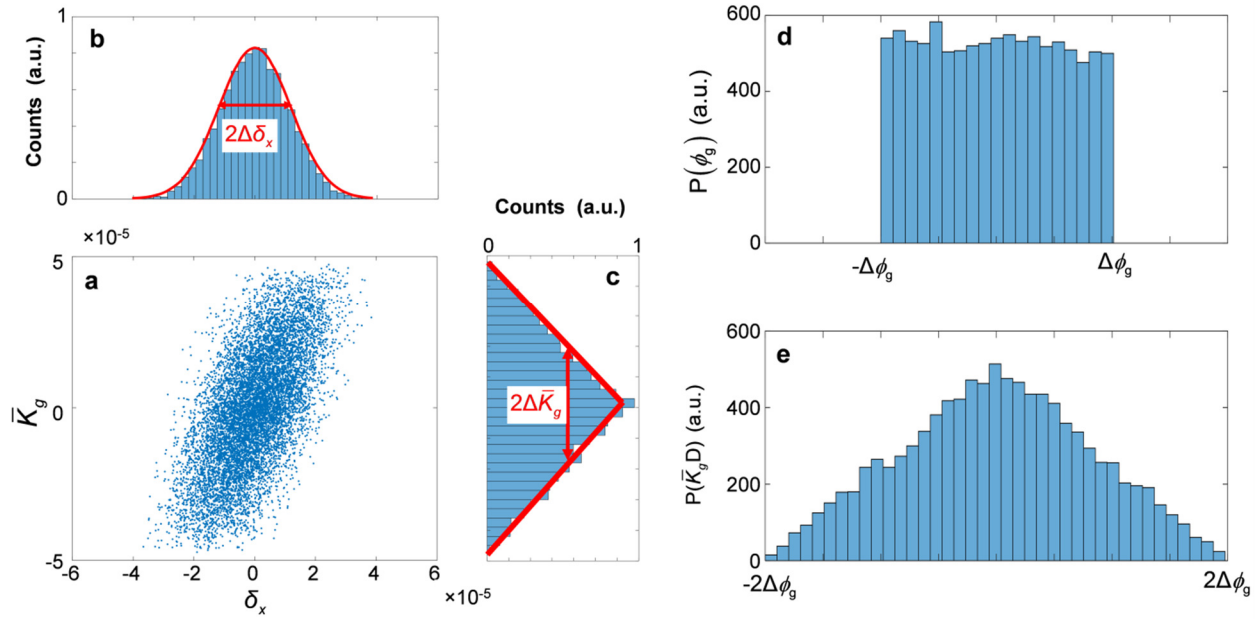
Supplementary Fig. 6. The approximated amplification factor in the weak measurement. **a**, The theoretical amplified PSHE as a function of β . In the shaded regions, the approximation $A_\beta \approx \bar{A}_\beta$ is valid, and the PSHE can be evaluated from the relation $\delta \approx A_\beta \delta / \bar{A}_\beta = (\langle k_y \rangle_\beta - \langle k_y \rangle_{-\beta}) / \bar{A}_\beta$. **b**, The theoretical curve of $(\langle k_y \rangle_\beta - \langle k_y \rangle_{-\beta}) / \bar{A}_\beta$ as a function of β . The dashed line denotes the spin shift, δ .



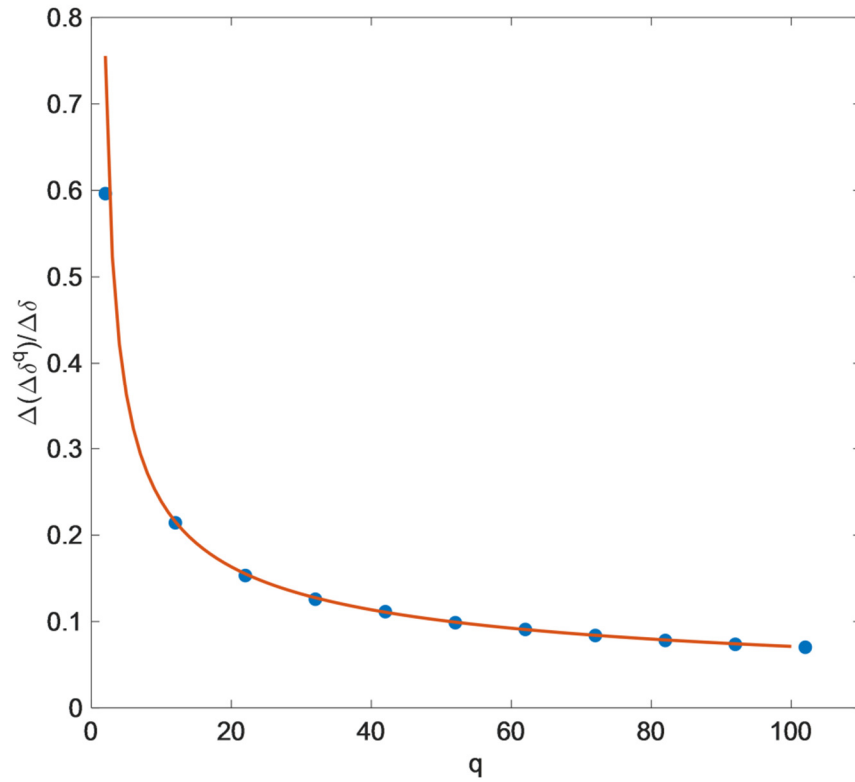
Supplementary Fig. 7. The measured hysteresses of the PSHEs. a-c, The measured PSHEs as a function of the external magnetic field for 1D (a) and 2D (b) disordered metasurfaces and a nickel film (c). The pink dots denote the results measured from $B = 0$ to $B = 100$ mT. The red dots denote the results measured from $B = 100$ mT to $B = -100$ mT. The blue dots denote the results measured from $B = -100$ mT to $B = 0$.



Supplementary Fig. 8. The magnetic-controlled formation of VPs in the near field of 2D disordered metasurfaces. **a**, The sketch of the experimental setup for measuring the near field of the metasurface. The SEM for a 2D disordered metasurface is shown. **b-d**, The calculated near-field distributions of a 2D disordered metasurface for different magnetizations $M = -1, 0,$ and $1,$ respectively. Top panel: the zoomed-in (marked by the white squares) phase and intensity distributions. The VPs are nanoscale optical topological defects with a pair of opposite phase singularities. **e-g**, The measured intensity distributions of the 2D disordered metasurfaces for different external magnetic fields. The insets depict the details of the magnetic-controlled dark-spot intensity changes. The blue curves are intensity distributions on the cut lines. The valleys on the curves indicate the defects.



Supplementary Fig. 9. The statistical probabilities of the PSHEs. **a**, The linear correlation between δ_x and \bar{K}_g . **b** and **c**, The probability distributions for δ_x (**b**) and \bar{K}_g (**c**). The data are calculated from 10^4 disordered metasurfaces with different realizations of the random function $f(x)$. The parameters for each metasurface are $D = 21\lambda$, $p = 0.6\lambda$, and $\Delta\phi_g = \pi \times 10^{-3}$. The curve in (**b**) is a fitted Gaussian function. **d**, The calculated probability distribution of $\phi_g(x) = \Delta\phi_g f(x)$. **e**, The calculated probability distribution of $\bar{K}_g D$, defined as $\phi_g(x_N) - \phi_g(x_1)$. Both $\phi_g(x_N)$ and $\phi_g(x_1)$ obey the flat probability distribution in (**d**).



Supplementary Fig. 10. The uncertainty of the estimated standard deviation from a statistical measurement with a number of q disorders. The curve shows the theoretical values obtained from Eq. S12. The dots are calculation results from Monte Carlo methods. Specifically, each dot is obtained by repeating statistical calculations for 10000 times, with each time conducting a number of q different disorders resulting in a value of $\Delta\delta^q$.